PHYSICAL REVIEW B **103**, 054433 (2021)

First-principles study of the electronic and magnetic properties of Fe, Co, and Ni dimers adsorbed on polycyclic-aromatic-hydrocarbon molecules as well as the laser chirp effect on the ultrafast spin dynamics

Meng-Lin Xie,[1] Yu-Ting Zheng,[1] Jing Liu,[2] Wei Jin,[1,*] Chun Li,[3] Georgios Lefkidis,[2,3] and Wolfgang Hübner[2]
[1] *School of Physics and Information Technology, Shaanxi Normal University, Xi'an 710119, China*
[2] *Department of Physics and Research Center OPTIMAS, Technische Universität Kaiserslautern, P.O. Box 3049, 67653 Kaiserslautern, Germany*
[3] *School of Mechanics, Civil Engineering and Architecture, Northwestern Polytechnical University, Xi'an 710072, China*

(Received 21 December 2020; accepted 2 February 2021; published 22 February 2021)

We investigate the geometric, electronic, and magnetic properties of TM_2(PAH) complexes [transition metal (TM) = Fe, Co, Ni; polycyclic-aromatic hydrocarbon (PAH) = $C_{10}H_8$, $C_{16}H_{10}$, $C_{24}H_{12}$, $C_{32}H_{14}$] as well as the optically induced ultrafast spin dynamics from a first-principles study. Geometrically, the magnetic dimer of each of the complexes [except for $Ni_2(C_{16}H_{10})$] turns out to prefer to adsorb above the hollow site of the outer carbon ring of the PAH molecule. The PAH-size effect and TM-element effect on the energy levels and spin localizations are analyzed. It is found that for the structures with the same PAH molecules, the level bands generally get wider from Fe via Co to Ni, while the number of spin-localized states overall decreases in the same order. For the structures with the same TM species [except for the two complexes $Ni_2(C_{16}H_{10})$ and $Fe_2(C_{32}H_{14})$], the low-lying levels are hardly affected by the size of the PAH molecules. Among all the calculated levels for each complex [except for $Ni_2(C_{16}H_{10})$], there are always more states with spin localized on the remote magnetic center than those localized on the near center. Driven by nonchirped subpicosecond laser pulses, a series of ultrafast spin-flip and spin-transfer scenarios on these structures are predicted and analyzed, based on which the laser chirp effect is further explored and some rules of thumb about the chirp tolerance and sensitivity are obtained. The results demonstrated in this paper are believed to enrich our understanding of the size- and structure-dependent electronic and magnetic properties of the carbon-based magnetic molecular structures, and further to promote the relevant experimental realization of the spin dynamics and their potential applications in future molecular spin devices.

DOI: 10.1103/PhysRevB.103.054433

I. INTRODUCTION

Motivated by the demanding quest for higher-density magnetic data storage in information technology and the ability of magnetism to be manipulated optically on ultrafast timescales [1–11], transition-metal (TM) nanoscopic structures, especially the TM molecular systems which possess ultimate small sizes, discrete energy levels, and large magnetic anisotropy, hold much promise for miniaturized magnetic logic elements and high-speed quantum information processing [12–15]. Numerous experimental and theoretical works about the TM clusters or molecules, both in the gas phase [16–18] and deposited on or embedded within suitable substrates {e.g., metallic surfaces [19,20] and carbon-based molecules such as carbon nanotubes [21], fullerenes [22,23], graphite [24], graphene [25–28], and polycyclic-aromatic hydrocarbons (PAHs) [29–38]}, have been devoted to the ultimate goal of their potential applications in nanospintronics devices.

In particular, the π-conjugated TM-PAH complexes have attracted considerable interest recently considering the availability of new experimental techniques to synthesize, the wide variety of their structural (due to the various π binding sites of PAHs for the attachment of metal atoms) and magnetic properties, and their potential applications as practical building blocks of novel nanomagnetic materials [36]. A series of joint experimental and density functional theory (DFT) based theoretical work on Fe/Co-coronene and Fe/Co-pyrene complexes, generated by laser vaporization techniques, in terms of their photoelectron spectroscopy, geometries, dissociation or ionization energies, and magnetic moments has been reported [29,30,33,35]. By using a similar DFT-related method, the interactions of Co adatoms, dimers, and tetramers with various PAH molecules ranging from benzene to circumcoronene [37,38] and the harmonic and anharmonic infrared spectra of Fe-coronene [34] have also been investigated. To treat the electron correlation more properly, Rudenko *et al.* [39] applied the complete-active-space self-consistent field approach to explore the adsorption of a single cobalt atom on graphene modeled by a molecule of coronene and found that far from the surface the correlations manifest themselves in weak attractive interactions of the van der Waals type, while in the vicinity of the surface the role of correlations become more pronounced, an effect that can be attributed mainly to the screening of the strong Coulomb repulsion between electrons in the *3d* shell. All these studies provide valuable insights

---

[*] jinwei@snnu.edu.cn

©2021 American Physical Society

into the adsorption properties, bonding characteristics, configuration stability, and electronic and magnetic properties of the TM-PAH systems and also bring some clues about the modification of the PAH molecules to improve the magnetic performance for future usage. However, to the best of our knowledge, little attention has been paid to the magnetodynamics or spin control between different electronic states for these carbon-based complexes, as one of the most important aspects towards nanospintronics applications. To explore this quantum mechanical issue, in the absence of experimental concern, a more accurate wave-function-based (instead of the DFT-based) theoretical study which is capable of (1) including both the static (relating to magnetization) and dynamical (relating to optical activity) correlations effectively, (2) calculating a sufficiently large number of accurate many-body excited states, and (3) performing spin manipulation among these states in a controllable way is essentially needed.

Previously, by using the high-level quantum chemistry method, we have investigated the laser-induced spin dynamics in the (half-)sandwich-like $(\mathrm{Fe/Co})_{1,2}(\mathrm{benzene})_{1,2}$ molecules as well as the laser and magnetic field effects [11,40], and obtained some promising and enlightening results for the guidance of future experiments. In this paper, under the same theoretical framework, we go further to explore the stabilities, electronic structures, spin localizations, and ultrafast spin functionalities in $\mathrm{TM}_2(\mathrm{PAH})$ complexes, where for the TM atoms the three elements Fe, Co, and Ni are chosen and, for the PAH molecules, naphthalene ($C_{10}H_8$), pyrene ($C_{16}H_{10}$), coronene ($C_{24}H_{12}$), and ovalene ($C_{32}H_{14}$) are chosen (here, even larger PAH molecules are not considered due to the huge computational cost caused by our high-level method). Through systematic investigation, we hope to address the following basic issues: (1) What are the geometric, electronic, and magnetic properties of these TM-PAH systems? (2) What are the PAH-size effect and TM-element effect on these properties? (3) How do these properties affect the achieved ultrafast spin dynamics? (4) What are the effects of chirped laser pulses on the scenarios? These inspections, in combination with our previous relevant study on TM-benzene systems, can help to enrich our fundamental understanding of the size- and structure-dependent magnetic properties as well as spin manipulation of the carbon-based molecular structures, stimulate relevant experimental efforts, and offer guidance for designing related spin functionality for future molecular spin-logic devices and quantum computers. In addition, PAHs can be considered as structural elements of graphene for studying the interaction with TM clusters. Especially when investigating the local properties of TM atoms adsorbed on an extended substrate such as graphene, e.g., the TM-substrate interactions, magnetic properties of TM atoms, and the local spin control, an exact description of the whole support structure is not always necessary since the bonding caused by the covalent interactions with *3d* TM atoms is essentially local [39]. One can see that some of our results concerning the geometries and ground-state spin localizations show good agreement with a series of DFT studies of TM_2-graphene systems [27,41–43]. Thus a systematic study on these finite-size TM-PAH complexes gives some hope to provide an accurate prediction of the magnetic nature and spin manipulation of the TM-graphene systems and to promote the experimental realization towards graphene-based (nano- or micro)spintronic devices in the near future.

The structure of the paper is as follows: Section II introduces the theoretical method and computational details. In Sec. III the optimized geometries of the investigated structures and the corresponding analysis of their configurations as well as some comparisons are presented. Then, the ground and excited electronic levels and spin localization analysis are given in Secs. IV and V, respectively, based on which in Sec. VI the achieved ultrafast dynamics results of spin-flip and spin-transfer scenarios as well as the chirp effects are presented. Our main findings are summarized in Sec. VII.

II. THEORETICAL METHOD

Our calculations are mainly divided into two parts: solving the many-electron problem and propagating the dynamical evolution. For the first part, we solve in two successive steps: the Hartree-Fock (HF) calculation for the geometric optimization and the symmetry-adapted-cluster configuration interaction (SAC-CI) method [44] for the many-body electronic structure. All these calculations are performed with the Gaussian 16 package [45], with the Lanl2dz basis set adopted for the TM atoms and STO-3G for the other atoms (the selection of these combined basis sets has been proven affordable and adequate for the description of the ligand-stabilized Ni_2 complex [46] through the good agreement with experiment). During the optimization, the threshold values of the maximum force component and the root mean square of all forces are set to 4.5×10^{-4} and 3.0×10^{-4} hartrees/bohr, respectively. After confirming the stability through the infrared spectra with no imaginary frequencies, in the subsequent SAC-CI calculations the lowest 10 or 20 triplet terms (depending on whether the symmetry of the structure is C_s or C_1) for each irreducible representation of the structures are calculated and prepared for the subsequent calculation of the dynamics. By considering the virtual excitations between various molecular orbitals obtained at the HF level, the multideterminantal SAC-CI ground and excited wave functions include both the static and dynamic correlations, which are significantly crucial for the description of strongly correlated systems, and thus are more accurate.

For the second part, to drive the spin dynamics flexibly, time-dependent sech^2-shaped laser pulses are applied, before which one additional step is taken, i.e., the inclusion of an external magnetic field (B field, for the Zeeman splitting) and spin-orbit coupling (SOC; for a more realistic description of the system and at the same time producing spin-mixed states as intermediate states to mediate the transitions, e.g., between two states with opposite spins; the process is also referred to as a Λ process [47]). Within the electric dipole approximation, we numerically solve the time-dependent coupled differential equations [46,48] using the fifth-order Runge-Kutta method combined with the Cash-Karp adaptive step size [49]. For a certain spin functionality, we selectively choose the appropriate initial and final states and optimize the laser parameters with a specially developed genetic algorithm [50]. Only the dynamics with desired fidelity (i.e., the final occupation of the targeted state) is considered as achievable.

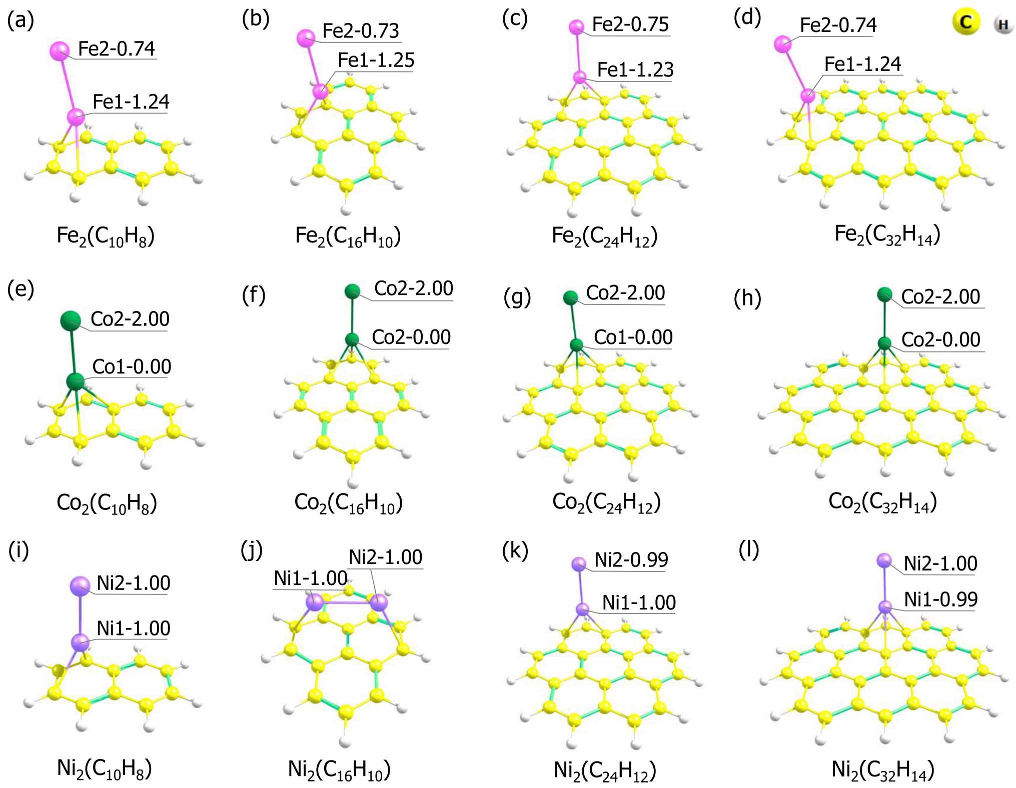

FIG. 1. The optimized geometries of TM_2(PAH) with spin multiplicity 3. (a) $Fe_2(C_{10}H_8)$, (b) $Fe_2(C_{16}H_{10})$, (c) $Fe_2(C_{24}H_{12})$, (d) $Fe_2(C_{32}H_{14})$, (e) $Co_2(C_{10}H_8)$, (f) $Co_2(C_{16}H_{10})$, (g) $Co_2(C_{24}H_{12})$, (h) $Co_2(C_{32}H_{14})$, (i) $Ni_2(C_{10}H_8)$, (j) $Ni_2(C_{16}H_{10})$, (k) $Ni_2(C_{24}H_{12})$, and (l) $Ni_2(C_{32}H_{14})$. The Mulliken spin-density values of the two magnetic centers TM1 and TM2 for each structure are indicated.

III. GEOMETRIES

The optimized structures of TM_2(PAH) (TM = Fe, Co, Ni; PAH = $C_{10}H_8$, $C_{16}H_{10}$, $C_{24}H_{12}$, $C_{32}H_{14}$) obtained at the HF level are shown in Fig. 1. For each complex, the PAH molecule is relaxed without symmetry constraint [37,43], and a large number of possible absorption sites are considered. To guarantee the stability of these geometries, the frequency calculations are subsequently performed. More details about the optimization and the infrared spectra can be found in Table S1 and Fig. S1 of the Supplemental Material [51], respectively. Here, considering the huge computational cost (especially when calculating the high-level excited states) for higher spin multiplicity, we restrict ourselves to triplet systems which have lower energies than the corresponding singlet ones.

Generally, two magnetic atoms can be arranged on the same side or different sides of each PAH molecule. However, in this paper we only consider the former case since kinetically it is more stable (see Sec. 1 of the Supplemental Material [51]) and technically it is easier to obtain. It also has been confirmed that the Fe and Co dimers prefer to adsorb on the same side of the graphenelike flakes in Refs. [29] and [38]. As can be seen from Fig. 1, the stabilized geometries of these structures exhibit two characteristics: (1) The magnetic dimers of the structures [except for $Ni_2(C_{16}H_{10})$] prefer positions vertically (loosely speaking) above the hollow sites of the hexagon carbon rings, which is in agreement with previous theoretical calculations in Refs. [11,27,37,38,40,42,43,52–54], and (2) the magnetic atoms tend to be on top of the outer ring of each PAH molecule, consistent with Refs. [29,36,38]. For the first characteristic, the graphenelike flakes exhibit acceptorlike character at hollow sites because of their delocalized π electrons [41], which thus leads to stronger and more stable TM-carbon bonds than the ones at other sites. For the origin of the second characteristic, usually, the outer ring has higher π electron content and aromaticity and thus is more likely to attract magnetic centers [29,36]. With respect to the symmetry, a magnetic center at the edge hollow site would lower the symmetry and gain more stability [38]. In addition, from Fig. 1 one can clearly see that the configurations of $TM_2(C_{10}H_8)$ or $TM_2(C_{24}H_{12})$ clusters exhibit similar geometries irrespective of the TM atoms, while for the support molecule $C_{16}H_{10}$, the adsorption sites of the three structures are all different (most striking is that the Ni dimer lies parallel to its carbon sheet), and for $C_{32}H_{14}$ the Fe_2 sits on the hollow site of a different outer ring from the other two complexes. More detailed investigation shows that, except for the parallel configuration $Ni_2(C_{16}H_{10})$ with a Ni-Ni bond of 2.598 Å, the TM-TM bond lengths lie in the ranges of 2.832–2.856, 2.571–2.58, and 2.457–2.46 Å for Fe_2(PAH), Co_2(PAH), and Ni_2(PAH), respectively, which therefore indicates that the TM-TM bond lengths for each magnetic species are almost unaffected by the PAH molecules. This to some extent relates to the theoretical estimation that the PAH molecules converge extremely slowly with the increase in the number of benzene rings since the gap between the highest occupied molecular orbital and the lowest

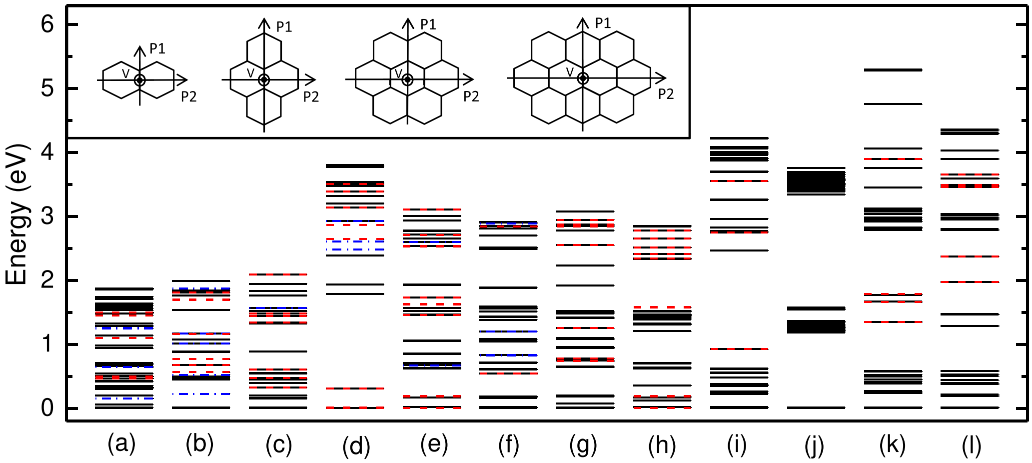

FIG. 2. (a)–(l) The 61 lowest-lying energy levels of the 12 structures obtained from the SAC-CI method after the inclusion of SOC and the magnetic field along the P1 direction (refer to the inset, in which the TM dimers on top of the PAH molecules are not shown for clarity). Among the levels for each structure, the blue dash-dotted lines denote the states with spin localized on TM1, and the red dashed lines denote the states with spin localized on TM2.

unoccupied molecular orbital (the HOMO-LUMO gap) in a large PAH molecule is found to close only at a cluster size of 1000 six-membered carbon rings [39,55].

The Mulliken spin-density values on the two magnetic centers obtained at the HF level for each structure are also given in Fig. 1. One can see that by comparing the relative spin-density values of the two magnetic centers, for each of the four ground-state Fe_2(PAH) complexes, spin is mainly localized on the near magnetic center Fe1 (the one near to the PAH plane), while for each of the four ground-state Co_2(PAH) complexes the magnetism is totally localized on the remote center Co2 (the one far away from the PAH plane, consistent with the findings in Refs. [27,28,37,38]). Similar results have also been found in our previous work [11,40], in which the spin-density values on the near and remote magnetic centers are 1.12 and 0.86 for $Fe_2(C_6H_6)$ and 0.00 and 2.00 for $Co_2(C_6H_6)$. The spin of each of the ground-state Ni_2(PAH) complexes, no matter whether the geometric configuration of the two Ni atoms is parallel or vertical, is always distributed equally, indicating a magnetic property similar to that of the free Ni dimer. This can be attributed to the dimerized tendency of the two Ni atoms for the vertical configurations (since the Ni-Ni distances are shorter and possess stronger couplings) and the indistinguishability of the two Ni atoms for the parallel configuration. Note that the dimerization tendency can also be observed if we compare with the bond length of the free Ni dimer obtained from the geometric optimization at the same HF level under the same spin multiplicity. In previous studies, for the stable configurations of the Ni dimer, two different ranges of bond lengths, i.e., 2.15–2.23 Å [56–60] and 2.56 Å [61,62], have been proposed. Here, in our calculation, three stable configurations at 2.18, 2.007, and 2.53 Å have also been obtained; however, the last configuration with bond length at 2.53 Å proves to be even lower in energy and more stable than the former two. Thus the Ni-Ni bonds of Ni_2(PAH) are relatively shortened compared with that of the bare Ni_2. Obviously, for the ground-state TM_2(PAH) complexes obtained at the HF level, although the geometric differences between the three types of magnetic species [except for $Ni_2(C_{16}H_{10})$] are minor, the magnetic properties of their TM dimers differ substantially, among which Co_2(PAH) complexes exhibit the largest changes compared with the corresponding free Co dimer. These findings, to some extent, agree with the conclusion that the similarity between $Fe_2(\text{coronene})^-$ and $Co_2(\text{coronene})^-$ in structures can induce dissimilar electronic structures and photoelectron spectra in Ref. [32].

In the next two sections, we will focus on the more accurate electronic structures of the systems obtained from the SAC-CI method and their spin localization distribution after including the SOC and adding an external magnetic field (with a strength of 10^{-5} a.u. = 2.35 T). As analyzed in our previous work [48], the spin properties of these states (e.g., spin magnitude and spin localization) strongly depend on the structures and the direction of the applied B field. For the subsequent calculations and discussions, only three typical directions for the B field (i.e., two parallel orientations and one vertical orientation with respect to the PAH planes, denoted by P1, P2, and V, respectively, as shown in the inset of Fig. 2) that are easily characterized and controlled in experiment will be selectively investigated.

IV. ELECTRONIC STRUCTURES

Figure 2 shows the lowest 61 ground and excited triplet levels of the 12 structures from the SAC-CI results after the inclusion of SOC and the application of the B field along the P1 direction (the levels for the other two B-field directions which exhibit almost the same patterns are not shown since the effect of the B direction on the energy values of the states is negligible on this scale). By comparing the level distributions of different structures [except for $Fe_2(C_{32}H_{14})$ and $Ni_2(C_{16}H_{10})$], we find that (1) the energy bands of the complexes with the same PAH molecules get wider and wider from Fe via Co to Ni. This trend is consistent with the observations in Refs. [48] and [63] and can be attributed to the cooperative effects of the magnetic species, electron numbers, and basis functions. Notably, there always exist relatively large energy gaps in Ni_2(PAH) compared with the corresponding Fe_2(PAH) and Co_2(PAH) structures. (2) The low-lying (e.g., below 0.7 eV) level distributions of the systems with the same magnetic species are generally hardly affected by the size of the PAH molecules [which is particularly evident for the four Co_2(PAH) and three Ni_2(PAH) complexes]. These two findings still hold if the two structures (with the lowest 61 states) $Fe_2(C_6H_6)$ and $Co_2(C_6H_6)$ [11,40] are included for comparison.

We note that the peculiar levels of $Ni_2(C_{16}H_{10})$, which mainly concentrate in three energy regions with two huge energy gaps, result from the parallel alignment of the Ni dimer above the $C_{16}H_{10}$ molecular plane, while the reason for the extraordinary electronic structure of $Fe_2(C_{32}H_{14})$, i.e., the extremely small number of states below 1.5 eV and the existence of a large gap of 1.48 eV between states 6 and 7 (which stem from the second and third triplet terms, respectively), however, is still unclear. For this, we have also additionally calculated the lowest 20 singlets for each structure (see Fig. S2 of the Supplemental Material [51]) to rule out the reason for ignoring singlets and tried a different configuration of $Fe_2(C_{32}H_{14})$ which lies 0.08 eV higher (the third configuration is shown in Table S1 of the Supplemental Material [51]) to exclude the singularity of the geometric configuration. The results show that for the former case (with the same level distribution trends as mentioned above) there are no singlets lying in this gap region for $Fe_2(C_{32}H_{14})$ and for the latter case the obtained level distributions still exhibit a similar pattern. Therefore, for $Fe_2(C_{32}H_{14})$, whether its unique level features originate from the intrinsic nature, or the exclusion of even higher spin states, or the inappropriate method used for treating such a structure, remains an open issue for further studies.

V. SPIN LOCALIZATIONS

It has been clear that the ultrafast spin dynamics achieved in a certain system is determined by the properties of its electronic structure [48], including the level distribution (which to some extent plays an important role in searching for proper intermediate states and thus affects the addressability of the dynamics) and the spin localization (which is structural and magnetic field dependent and affects the choice of promising initial and final states and thus the types of spin functionalities). Next, to fully understand the feature of the achieved spin dynamics to be discussed in the following section, we explore further the spin localizations of these many-body states under all three B directions in great detail.

Table I gives the distribution (i.e., the percentage values) of the spin-localized states among the total 61 states for each of the 12 structures under three different B-field directions, from which one can clearly see that for each structure [except for $Co_2(C_{16}H_{10})$ with field along the P1 and V directions] there are always more states with spin localized on the remote magnetic center (TM2) than states with spin localized on the near one (TM1), which is also true for the clusters $Fe_2(C_6H_6)$ and $Co_2(C_6H_6)$ [11,40]. This can also be clearly observed from Fig. 2 in the case of the magnetic field orientated along the P1 direction, in which the number of red dashed lines, denoting the states with spin localized on TM2, is larger than the number of blue dash-dotted lines, denoting the states with spin localized on TM1. Here, a spin-localized state is one that satisfies the following: (1) The sum of its density values on the two magnetic centers is larger than 0.8 (the states with lower values are found to have always small spin expectation values and thus are not considered as promising candidates as initial or final states for spin dynamics), and (2) the spin-density value on one magnetic center occupies at least 80% of the total. Note that the maximal sum of the spin densities on all the atoms for each structure is 2 since we consider triplet systems with two unpaired electrons. The spin densities on the carbon sheets for the dimer complexes are not worth considering here since the values are found to be always small for both the ground and excited states (which is also consistent with the statements in Refs. [27,38] that graphene carries less magnetism for TM-graphene systems). The maximal spin-density value of the PAH molecules, when considering all the states of the 12 structures under the application of the three magnetic field directions, is 0.154, the value for the complex $Fe_2(C_{32}H_{14})$ under the application of the vertical magnetic field.

TABLE I. The distribution of the spin-localized states on different magnetic centers among the total 61 states for each of the 12 structures for the three typical B-field directions. Values are percentages.

B-field direction	PAH	Fe_2(PAH)		Co_2(PAH)		Ni_2(PAH)	
		Fe1	Fe2	Co1	Co2	Ni1	Ni2
P1	$C_{10}H_8$	9.8	16.4	6.6	26.2	0.0	9.8
	$C_{16}H_{10}$	21.3	26.2	9.8	6.6	0.0	0.0
	$C_{24}H_{12}$	3.3	26.2	0.0	23.0	0.0	13.1
	$C_{32}H_{14}$	13.1	31.2	0.0	26.2	0.0	16.4
P2	$C_{10}H_8$	11.5	24.6	8.2	9.8	0.0	16.4
	$C_{16}H_{10}$	21.3	27.9	3.3	23.0	0.0	0.0
	$C_{24}H_{12}$	4.9	26.2	4.9	26.2	0.0	6.6
	$C_{32}H_{14}$	11.5	37.7	3.3	19.7	0.0	23.0
V	$C_{10}H_8$	14.8	24.6	6.6	9.8	0.0	13.1
	$C_{16}H_{10}$	24.6	27.9	8.2	4.9	0.0	0.0
	$C_{24}H_{12}$	3.3	16.7	6.6	19.7	0.0	6.6
	$C_{32}H_{14}$	13.1	23.0	3.3	13.1	0.0	16.4

For the systems with the same PAH molecules, one finds that the percentage values of the spin-localized states (the sum of those on TM1 and on TM2) overall decrease from Fe via Co to Ni [with the exceptions that $Co_2(C_{10}H_8)$ possesses a slightly higher percentage value than $Fe_2(C_{10}H_8)$ when the B field is along the P1 direction and $Co_2(C_{24}H_{12})$ possesses a slightly higher percentage value than $Fe_2(C_{24}H_{12})$ when the B field is along the V direction] under all three B-field directions. Among all the cases, the spin localization of $Fe_2(C_{16}H_{10})$ is always the best (with respect to its largest and balanced percentage values for the spin-localized states), and the spin localization of $Ni_2(C_{16}H_{10})$ is always the worst due to its geometrical configuration. For the systems with the same TM species, however, the PAH effect on the spin localization is not obvious and thus is not discussed here.

The feature of spin-density distribution plays a significant role in determining the realization of spin functionality on these structures. One can deduce that the Fe structures, which possess more profound spin-localized states, are more promising in achieving spin-transfer scenarios, which indeed is confirmed by our later calculations. Here, it should be noted that for $Fe_2(C_{24}H_{12})$, although its spin-localized states are more numerous, the unbalanced distribution of the states localized on the two Fe atoms (in particular, spin-localized states on Fe1 are extremely rare) makes spin transfer hardly achievable. A similar situation can also be found for $Co_2(C_{24}H_{12})$, $Co_2(C_{32}H_{14})$, and the four Ni structures when the B field is along the P1 direction; that is, none of them has spin states localized on TM1, and thus no transfer is expected to be found (this is also true for the other two B directions, even if the two Co structures do have a small number of spin states localized on Co1).

It should be emphasized that after including the electron correlations by considering the virtual excitations between the HF molecule orbitals and the multideterminant expansions for the SAC-CI wave functions, the spin-density values of the SAC-CI ground states are to some extent different from the ones indicated in Fig. 1. However, if we compare only the relative spin-density values of the two magnetic centers (without considering the above spin localization criteria), the spin localizations obtained at the SAC-CI level are the same as the ones at the HF level, with only one exception—$Fe_2(C_{32}H_{14})$, in which the SAC-CI ground state becomes mainly distributed on the remote Fe atom. This can be attributed to the fact that its main contributing virtual excitations are not simple single excitations like the others but a few double excitations between various molecular orbitals with different electron-cloud characters (e.g., *p* type or *d* type) and different localizations. After taking all these complicated excitations into account in the state expansions, our results show that when the magnetic field is applied along the P1 direction, the spin-density values on the near and remote magnetic centers for the SAC-CI ground-state of $Fe_2(C_{32}H_{14})$ are 0.045 and 1.195, respectively; thus the spin localization is on Fe2 (see Fig. 2). Under the same B-field direction, the spin-density values on the two magnetic centers (TM1, TM2) for the ground states of the four structures $Fe_2(C_{10}H_8)$, $Fe_2(C_{16}H_{10})$, $Co_2(C_{10}H_8)$, and $Co_2(C_{32}H_{14})$ are (1.26, 0.44), (1.41, 0.56), (0.00, 1.47), and (0.00, 1.75), respectively, which shows that they possess a localization distribution very similar to that obtained at the HF level (the values for the latter two structures can also be seen in Table S2 of the Supplemental Material [51]). For the rest of the structures, subject to the magnetic anisotropy, their spin-density values are very small under the B field along the P1 direction due to either the inappropriate magnetic field directions or relatively weak field magnitudes [48]. It has been found that when the magnetic field is applied along the P2 direction, the spin-density values on (TM1, TM2) for the SAC-CI ground states of $Fe_2(C_{24}H_{12})$, $Co_2(C_{16}H_{10})$, and $Co_2(C_{24}H_{12})$ increase up to (0.99, 0.27), (0.00, 1.49), and (0.00, 1.33), respectively, while for the four Ni complexes, the spin-density values of the ground states can be enhanced when the field strength increases. Take the SAC-CI ground state of $Ni_2(C_{10}H_8)$, for example: When the B field is four times larger along the P1 direction, its spin-density values of (Ni1, Ni2) can be increased from (0.130, 0.132) up to (0.542, 0.549), with the spin almost equidistributed on the two Ni atoms.

VI. LASER-INDUCED ULTRAFAST SPIN DYNAMICS

A. Spin-flip scenarios

In this section we present the laser-induced ultrafast spin dynamics achieved in these structures. First we discuss the nonchirped-laser-driven spin-flip scenarios, the initial and final states of which have (quasi)opposite spin directions. Since this type of spin functionality is not novel and has been analyzed previously, here we will not go into detail but will focus on the effect of electronic structures and spin localizations on the dynamics and the related laser parameters (more specifically, the laser energy). Figures 3(a)–3(l) show the spin-flip scenarios obtained in the 12 structures, among which the scenario in $Ni_2(C_{16}H_{10})$ is a global one due to the indistinguishability of the two Ni centers. Here, for each structure, several other spin-flip scenarios are also achievable (some of which may be more local and efficient). However, for the purpose of experimental implementation, only the one with the initial and final states being as low as possible in energy, under the prerequisite of its realizability, is shown. We find that when the initial and final states are chosen as states $|1\rangle$ and $|2\rangle$, the flip scenarios for the four structures Co_2(PAH) can all be realized with appropriate B-field directions (i.e., P1 or P2; see Table II). This is because all these ground states have pronounced spin localizations (see Table S2 of the Supplemental Material [51]) and several neighboring electronic states (see Fig. 2) that facilitate Λ-process-based scenarios.

For the Fe and Ni dimer complexes, the initial and final states of the achieved spin-flip dynamics all possess higher energies, due to the fact that either their ground states or lower excited states are not spin-localized states according to the spin-density criteria set for dynamics [e.g., for Fe_2(PAH) and Ni_2(PAH) with PAH = $C_{10}H_8$, $C_{16}H_{10}$, $C_{24}H_{12}$] or the lower spin-localized states are not suitable as the initial and final states for spin flip since their spin directions are not quasiopposite [e.g., for $Fe_2(C_{32}H_{14})$ and $Ni_2(C_{32}H_{14})$]. Additionally, for $Fe_2(C_{32}H_{14})$, although some of its ground and lower excited terms are both spin localized and potentially suitable as initial and final states, due to the absence of the intermediate states in their vicinities (as can be seen from the level distribution in Fig. 2), the relevant spin flip dynamics is unprocurable. Instead, a spin-flip scenario from state $|25\rangle$ to state $|27\rangle$, which stem from the eighth excited term with energy around 2.86 eV and have quasiopposite spin directions, is achieved.

The laser parameters for driving these scenarios are listed in Table II. Detailed inspection shows that the optimized laser energies for the spin-flip scenarios strongly depend on the involved intermediate states. For instance, for the flip scenarios in Figs. 3(a), 3(c), 3(e), 3(j), and 3(l), the corresponding energy differences between the initial and the dominant involved intermediate states (i.e., the intermediate states with higher or noticeable occupations during the propagation of the dynamics as indicated in Fig. 3) are $\Delta E_{|29\rangle,|5\rangle} = 0.78$ eV, $\Delta E_{|23\rangle,|10\rangle} = 0.23$ eV, $\Delta E_{|27\rangle,|1\rangle} = 1.51$ eV, $\Delta E_{|26\rangle,|4\rangle} = 0.38$ eV, and $\Delta E_{|25\rangle,|4\rangle} = 2.19$ eV, respectively, which are very close to their respective optimized laser energies, 0.82, 0.23, 1.52, 0.40, and 2.21 eV, as shown in Table II. For the others, the laser energies are largely determined by the energy differences between the initial (or final)

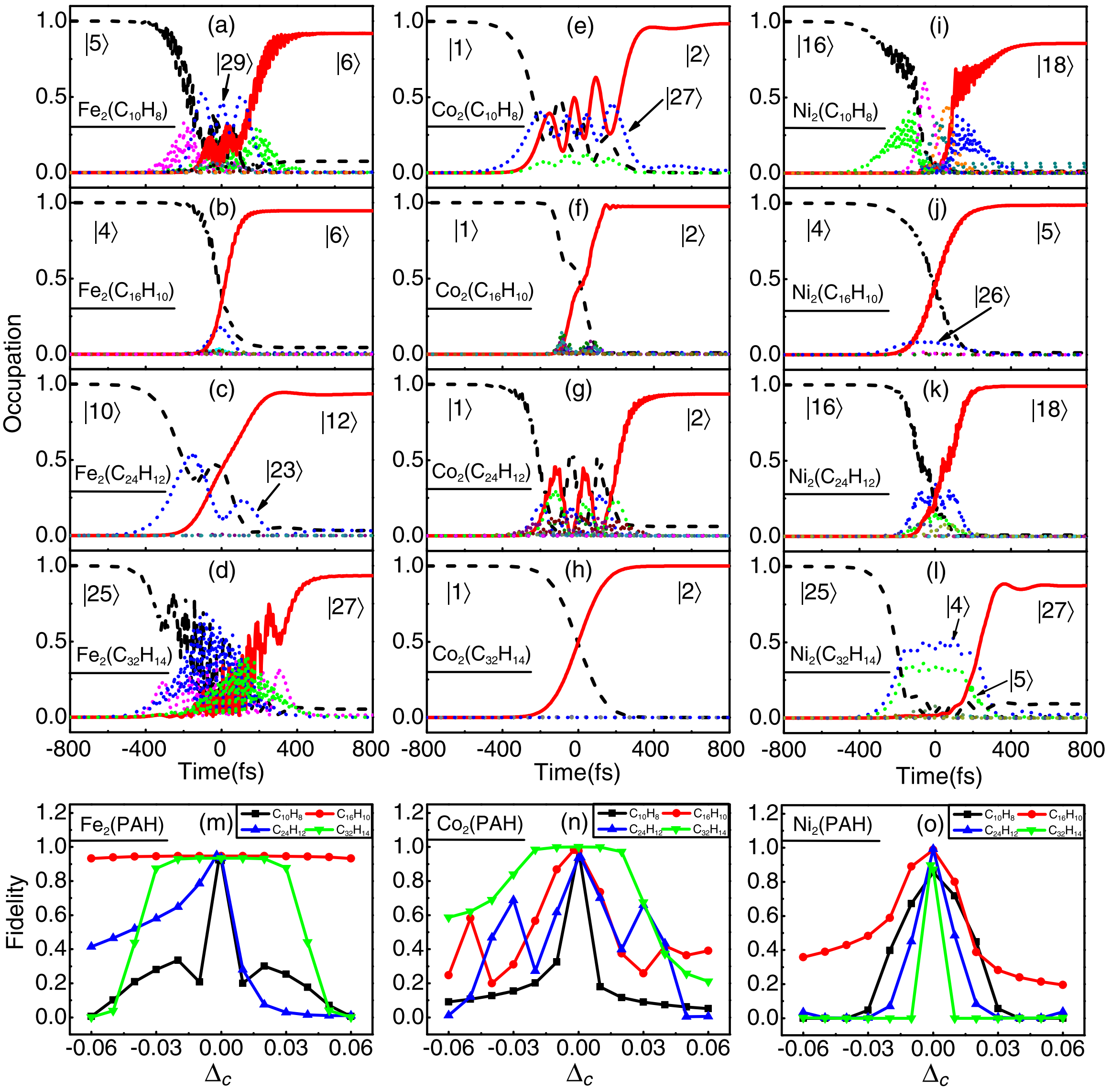

FIG. 3. Nonchirped-laser-driven ultrafast spin-flip scenarios and the corresponding laser chirp effects. (a)–(l) show the spin flip in $Fe_2(C_{10}H_8)$, $Fe_2(C_{16}H_{10})$, $Fe_2(C_{24}H_{12})$, $Fe_2(C_{32}H_{14})$, $Co_2(C_{10}H_8)$, $Co_2(C_{16}H_{10})$, $Co_2(C_{24}H_{12})$, $Co_2(C_{32}H_{14})$, $Ni_2(C_{10}H_8)$, $Ni_2(C_{16}H_{10})$, $Ni_2(C_{24}H_{12})$, and $Ni_2(C_{32}H_{14})$, respectively. (m)–(o) show the laser chirp effects for the flip scenarios in Fe_2(PAH), Co_2(PAH), and Ni_2(PAH), respectively. Detailed information on the initial and final states for these spin-flip scenarios can be found in Table S2 of the Supplemental Material [51].

states and the averaged energy values of all the intermediate states [in some cases, i.e., Fig. 3(b), the difference between the initial or final state and the highest intermediate state].

B. Spin-transfer scenarios

By choosing all possible initial and final states within the calculated level ranges with different spin localizations, we find that for all three B-field directions, spin-transfer scenarios, driven by nonchirped laser pulses, can always be achieved in $Fe_2(C_{10}H_8)$, $Fe_2(C_{16}H_{10})$, and $Fe_2(C_{32}H_{14})$. For $Fe_2(C_{24}H_{12})$, since there are only two (for the B field along the directions of P1 and V, the former case of which can be clearly seen from the blue dash-dotted lines in Fig. 2) or three (for the B field along P2) states localized on the Fe1 atom, none of the transfer scenarios has been found so far. Among all attempts for Co_2(PAH), spin transfer is only achieved in $Co_2(C_{16}H_{10})$ when the B field is applied along P1. We attribute this fact to their less spin-localized states or unbalanced spin localizations on the two magnetic centers. Remarkably, as shown in Fig. 2, no spin-localized states on Co1 exist in $Co_2(C_{24}H_{12})$ and $Co_2(C_{32}H_{14})$. For the four structures of Ni_2(PAH), due to the lack of spin-localized states [for $Ni_2(C_{16}H_{10})$] and spin states localized on Ni1 centers [for $Ni_2(C_{10}H_8)$, $Ni_2(C_{24}H_{12})$, and $Ni_2(C_{32}H_{14})$] for all three B directions, spin transfer is by no means possible. Next we choose one specific B-field direction, i.e., P1, to illustrate the features of the obtained spin-transfer scenarios.

We find that under the application of the B field along the P1 direction, in total 2, 12, 4, and 2 different transfer scenarios have been achieved in the structures $Fe_2(C_{10}H_8)$, $Fe_2(C_{16}H_{10})$, $Fe_2(C_{32}H_{14})$, and $Co_2(C_{16}H_{10})$, respectively.

TABLE II. The fidelity of the nonchirped-laser-driven ultrafast spin-flip and spin-transfer scenarios in the TM_2(PAH) complexes and the corresponding optimized parameters of the laser pulses. θ and ϕ denote the angles of incidence in spherical coordinates, γ is the angle between the polarization of the light and the optical plane, FWHM is the full width at half maximum of the laser pulses, and chirp is the factor by which the laser frequency changes linearly between $t = -\text{FWHM}/2$ and $t = +\text{FWHM}/2$; for example, 1 means the laser is nonchirped, 1.1 means the pulse frequency increases by 10% with time, and 0.9 means the pulse frequency decreases by 10% with time. The chirp values given in parentheses are the ones that give enhanced dynamics fidelity (the corresponding values are also given in parentheses) when investigating the chirp effect in Sec. VI C.

						Laser parameters						
Scenario		Structure	B-field direction	Process	Fidelity (%)	θ (deg)	ϕ (deg)	γ (deg)	Amplitude (arb. units)	FWHM (fs)	Energy (eV)	Chirp
Spin flip	(a)	$Fe_2(C_{10}H_8)$	P1	$\vert 5\rangle \rightarrow \vert 6\rangle$	91.9 (92.5)	7.7	95.6	248.0	0.0095	399.1	0.82	1.000 (0.999)
	(b)	$Fe_2(C_{16}H_{10})$	P1	$\vert 4\rangle \rightarrow \vert 6\rangle$	94.7	77.6	251.7	321.9	0.0074	306.4	2.15	1.000
	(c)	$Fe_2(C_{24}H_{12})$	P1	$\vert 10\rangle \rightarrow \vert 12\rangle$	93.7 (95.2)	211.7	131.7	331.4	0.0045	461.0	0.23	1.000 (0.998)
	(d)	$Fe_2(C_{32}H_{14})$	P1	$\vert 25\rangle \rightarrow \vert 27\rangle$	93.4	125.1	148.3	170.9	0.0027	425.1	0.36	1.000
	(e)	$Co_2(C_{10}H_8)$	P1	$\vert 1\rangle \rightarrow \vert 2\rangle$	98.2	167.7	176.0	69.9	0.0033	495.4	1.52	1.000
	(f)	$Co_2(C_{16}H_{10})$	P2	$\vert 1\rangle \rightarrow \vert 2\rangle$	97.6 (98.3)	258.8	316.8	223.3	0.0035	310.3	1.13	1.000 (0.998)
	(g)	$Co_2(C_{24}H_{12})$	P2	$\vert 1\rangle \rightarrow \vert 2\rangle$	93.9	274.8	130.8	352.8	0.0063	429.0	1.76	1.000
	(h)	$Co_2(C_{32}H_{14})$	P1	$\vert 1\rangle \rightarrow \vert 2\rangle$	100.0	42.9	114.4	221.1	0.0050	499.7	1.72	1.000
	(i)	$Ni_2(C_{10}H_8)$	P1	$\vert 16\rangle \rightarrow \vert 18\rangle$	85.6	335.5	38.2	196.8	0.0094	370.1	1.53	1.000
	(j)	$Ni_2(C_{16}H_{10})$	V	$\vert 4\rangle \rightarrow \vert 5\rangle$	98.7	236.1	343.8	272.5	0.0058	396.7	0.40	1.000
	(k)	$Ni_2(C_{24}H_{12})$	P1	$\vert 16\rangle \rightarrow \vert 18\rangle$	99.2	283.4	351.8	77.4	0.0081	328.6	0.59	1.000
	(l)	$Ni_2(C_{32}H_{14})$	P1	$\vert 25\rangle \rightarrow \vert 27\rangle$	87.3 (89.8)	183.7	310.0	208.2	0.0099	378.5	2.21	1.000 (0.999)
Spin transfer	(a)	$Fe_2(C_{10}H_8)$	P1	$\vert 16\rangle \rightarrow \vert 34\rangle$	80.4 (83.1)	49.1	32.8	155.7	0.0051	328.3	0.79	1.000 (1.001)
	(b)	$Fe_2(C_{16}H_{10})$	P1	$\vert 4\rangle \rightarrow \vert 22\rangle$	87.3 (87.6)	258.6	307.3	130.9	0.0066	361.5	0.63	1.000 (1.004)
	(c)	$Fe_2(C_{32}H_{14})$	P1	$\vert 18\rangle \rightarrow \vert 36\rangle$	81.5 (82.8)	185.8	128.0	34.1	0.0100	374.9	0.67	1.000 (1.001)
	(d)	$Co_2(C_{16}H_{10})$	P1	$\vert 16\rangle \rightarrow \vert 53\rangle$	98.1	42.7	179.2	29.4	0.0052	453.0	1.01	1.000

Here, only the scenarios with the initial and final states belonging to different triplet terms are counted; for example, for $Fe_2(C_{16}H_{10})$ the transitions $|4\rangle \rightarrow |22\rangle$ and $|5\rangle \rightarrow |23\rangle$ are considered as one since states $|4\rangle$ and $|5\rangle$ and states $|22\rangle$ and $|23\rangle$ are both from the same triplet terms, respectively. The larger number of spin-transfer scenarios obtained in $Fe_2(C_{16}H_{10})$ can be attributed to its higher and balanced percentage values of spin-localized states on Fe1 and Fe2, as analyzed in Sec. V. By contrast, for the other three structures, their unbalanced spin-localized states in the two magnetic atoms causes the much fewer achieved transfer scenarios.

Figures 4(a)–4(d) selectively show one of the achieved transfer scenarios for each of the four structures when the B field is applied along P1. The corresponding laser parameters of the four spin-transfer scenarios are listed in Table II. It is found that the optimized laser energies of the spin-transfer scenarios are mostly determined by the energy differences between the initial and final states, which is different from the case for spin-flip scenarios. For instance, the laser energies required for driving the spin-transfer dynamics in $Fe_2(C_{10}H_8)$, $Fe_2(C_{16}H_{10})$, and $Fe_2(C_{32}H_{14})$ are 0.79, 0.63, and 0.67 eV, respectively (see Table II), which are very close to the respective energy differences $\Delta E_{|34\rangle,|16\rangle} = 0.80$ eV, $\Delta E_{|22\rangle,|4\rangle} = 0.54$ eV, and $\Delta E_{|36\rangle,|18\rangle} = 0.66$ eV. For the transfer scenario in $Co_2(C_{16}H_{10})$ which involves only three intermediate states (among which state $|40\rangle$ with energy 1.88 eV acts as the dominant one and exhibits noticeable occupation during the propagation), since the initial and final states (with an energy difference of 2.02 eV) are far from each other, it goes through a quasi-two-step process (i.e., the Ξ process), and thus the optimized laser energy (1.01 eV, as shown in Table II) is close to $\Delta E_{|40\rangle,|16\rangle} = 1.06$ eV or $\Delta E_{|53\rangle,|40\rangle} = 0.96$ eV.

C. Laser chirp effect

Considering the fact that in reality some laser frequency chirp is inevitable and can hardly be suppressed, it is of great necessity that we explore the effect of the chirp on the performance of the population transfer. The state transitions in various two-level atomic systems using linear chirped laser pulses and their dependence on the chirping characteristics have been investigated intensively [64–67]. For the transitions in many-body level systems, the laser chirp impact on the ultrafast laser-induced local spin flipping on sodium-atom-bridged, homodinuclear magnetic molecules [68] and the analytical treatment of the model Λ processes driven by chirped lasers [69] have been reported. All these studies have revealed that the laser chirp has a significant effect on the rate and maximum of the population transfer; for example, the increase in the chirping parameter can decrease the probability of transition, reduce the spin moment, and sometimes serve as a manipulation tool for some functionality. In this section, we investigate the influence of the laser chirp on the fidelity of the achieved spin-flip and spin-transfer scenarios, aiming at finding some rules of thumb for these specific TM_2(PAH) systems and providing guidance for experimental realization.

Our linearly chirped laser pulse has the form $E(t) \propto \exp[i(\omega_0 t + \alpha t^2)]$, where ω_0 is the laser carrier frequency, $\alpha = \Delta_c\omega/\text{FWHM}$ is the frequency change rate, and the factor $\Delta_c = \text{chirp} - 1$ is a chirp parameter (i.e., chirp = 1 means the laser is nonchirped, 1.1 means the pulse frequency linearly increases by 10% with time, and 0.9 means pulse frequency linearly decreases by 10% with time). In the calculation, we keep the values of the other optimized laser parameters (i.e., θ, ϕ, γ, amplitude, FWHM, and energy) fixed and solely

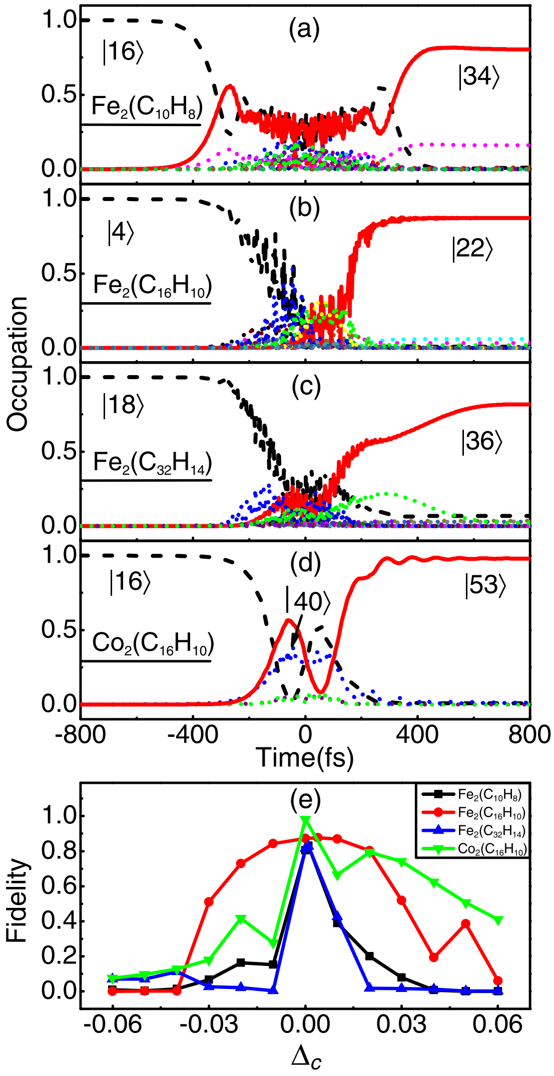

FIG. 4. Nonchirped-laser-driven ultrafast spin-transfer scenarios and the corresponding laser chirp effect. (a)–(d) show the spin transfer in Fe$_2$(C$_{10}$H$_8$), Fe$_2$(C$_{16}$H$_{10}$), Fe$_2$(C$_{32}$H$_{14}$), and Co$_2$(C$_{16}$H$_{10}$), respectively. (e) shows the laser chirp effects for the transfer scenarios achieved in the four structures. Detailed information on the initial and final states for these spin-transfer scenarios can be found in Table S2 of the Supplemental Material [51].

examine how the dynamics fidelity varies with Δ_c. The results are shown in Figs. 3(m)–3(o) and Fig. 4(e). For the spin-flip scenarios, we see the following: (i) When introducing the laser chirp increasingly in both the positive and negative directions, the fidelity of each of the scenarios gets overall suppressed {further study shows that the fidelity of the flip scenario in Fe$_2$(C$_{16}$H$_{10}$) drops below 0.4 when the pulse frequency increases by 11% or decreases by 12% with time, as shown in Fig. S3 of the Supplemental Material [51]}. (ii) Different magnetic species exhibit distinct tolerance or sensitivity features with respect to the laser chirp. Specifically, the stability (or the chirp tolerance) order for the flip scenarios of the structures with the same PAH molecules follows Fe > Co > Ni [the exception is Ni$_2$(C$_{10}$H$_8$), for which the spin flip has a higher chirp tolerance than Co$_2$(C$_{10}$H$_8$)]. Here, the chirp value is considered tolerable if the fidelity of the scenario keeps around or above 75%. (iii) For the structures with the same TM atoms, the chirp tolerances for the flip scenarios in Fe and Co structures both increase from C$_{10}$H$_8$ via C$_{24}$H$_{12}$ to C$_{32}$H$_{14}$, while for the Ni structures the order becomes reversed [i.e., the chirp-tolerance order becomes Ni$_2$(C$_{10}$H$_8$) > Ni$_2$(C$_{24}$H$_{12}$) > Ni$_2$(C$_{32}$H$_{14}$)]. (iv) While the fidelity changes of most of the flip scenarios are symmetric with respect to laser chirp in the two directions, the fidelity changes of the three structures Fe$_2$(C$_{24}$H$_{12}$), Co$_2$(C$_{32}$H$_{14}$), and Ni$_2$(C$_{16}$H$_{10}$) show asymmetric features; that is, their fidelity values get suppressed more strongly (and thus are more sensitive) for the positively chirped pulse.

As for the effect of laser chirp on spin-transfer scenarios, we see that the chirp-tolerance values increase in the order Fe$_2$(C$_{32}$H$_{14}$) $\approx$ Fe$_2$(C$_{10}$H$_8$) < Co$_2$(C$_{16}$H$_{10}$) < Fe$_2$(C$_{16}$H$_{10}$), which can be seen from Fig. 4(e). Fe$_2$(C$_{16}$H$_{10}$), for which the spin flip is most stable with the change in laser chirp, also has the largest chirp-tolerance value (from −1.8% to +2.2%) for its spin-transfer scenario. Therefore this structure, in combination with the fact that many more transfer scenarios have been achieved, can be considered as the most promising one for future molecular spintronic device design and applications. One additional remark regarding the sensitivity to the chirp that should be emphasized here is that both the insensitive and sensitive behavior of the dynamics might be useful in experiment, since the former helps to find stable conditions for spin dynamics while the latter may give better spatial addressability. In addition, for the asymmetric change in the fidelity with respect to the change in laser chirp in the two directions, the spin-transfer dynamics gets suppressed more strongly in the negative direction of the chirp change, showing exactly the opposite feature compared with the spin-flip scenarios which are more sensitive to the positive direction of change.

It should be noted that, as shown by the fidelity and chirp values given in parentheses in Table II, it is not always the case that the nonchirped laser is the optimal one to obtain the maximal population transfer for the dynamics (which, however, does not contradict the overall suppression trend of the fidelity with the increase in the chirp degree). It turns out that, driven by the negatively chirped laser pulses with $\Delta_c =$ −0.1, −0.2, −0.2, and −0.1%, the fidelity of the four spin-flip scenarios in Figs. 3(a), 3(c), 3(f), and 3(l) can increase by 0.6, 1.5, 0.7, and 2.5%, respectively, while for the three spin-transfer scenarios in Figs. 4(a)–4(c), the fidelity values can increase by 2.7, 0.3, and 1.3% using the positively chirped lasers with $\Delta_c =$ +0.1, +0.4, and +0.1%, respectively. This indicates that under some circumstances the fidelity of the ultrafast spin dynamics can be enhanced, although the improvement is limited, by the application of the chirped laser pulses (only with small deviations from the nonchirped ones).

VII. SUMMARY

We present a systematic *ab initio* study on the geometries, electronic structures, magnetic properties, and laser-induced ultrafast spin dynamics as well as the chirp effect in TM$_2$(PAH) complexes (TM = Fe, Co, Ni; PAH = C$_{10}$H$_8$, C$_{16}$H$_{10}$, C$_{24}$H$_{12}$, C$_{32}$H$_{14}$). Through the exploration of the geometric configurations, level distributions, and spin localizations of the 12 structures, some general trends regarding the PAH-size effect and TM-element effect are found, and their connections to the achieved spin dynamics are revealed. The results are summarized as follows:

(1) Except for $Ni_2(C_{16}H_{10})$, in which the Ni dimer lies parallel to the $C_{16}H_{10}$ plane, the magnetic dimer of each of the other complexes prefers to bind vertically (loosely speaking) above the hollow site of the edged carbon ring of the PAH molecule due to the acceptorlike character and higher stability of these adsorption sites.

(2) For the structures with the same PAH molecules [except for $Fe_2(C_{32}H_{14})$], the energy bands of the calculated SAC-CI levels get wider in the order Fe, Co, and Ni, while for the structures with the same magnetic species, the low-lying levels mostly exhibit quite similar distribution features irrespective of the size of the PAH molecule.

(3) For the spin localizations of the SAC-CI states, the number of spin-localized states overall decreases from Fe via Co to Ni for the structures with the same PAH molecules. The ground-state spin localization, independent of their geometric configurations, is also determined by the magnetic species. Specifically, the ground states of Fe_2 complexes [except for $Fe_2(C_{32}H_{14})$] are localized mainly on the near Fe center, the ground states of the four Co_2 complexes are localized on the remote Co centers, and those of Ni_2 complexes are always equally localized on the two Ni centers. Overall, among all the calculated SAC-CI ground and excited states, the number of spin-localized states on the remote magnetic center for each of the structures [except for $Ni_2(C_{16}H_{10})$] is always greater than that on the near magnetic center.

(4) Driven by appropriate unchirped laser pulses, ultrafast spin-flip scenarios are achievable in all of the structures, while spin-transfer scenarios can only be achieved in $Fe_2(C_{10}H_8)$, $Fe_2(C_{16}H_{10})$, $Fe_2(C_{32}H_{14})$, and $Co_2(C_{16}H_{10})$. The rest, due to the lack of or the much fewer spin states localized on TM1 centers, are not suitable for performing spin transfer. The realizability and features of the dynamics in this series of structures are found to strongly depend on the cooperative effects of their level distributions and spin localizations. The required laser energies for the flip scenarios are closely related to the involved intermediate states, while for the transfer scenarios they are largely determined by the energy differences between the initial and final states. The evidence so far suggests that the systems with favorable and balanced spin localizations possess more opportunities for obtaining richer spin dynamics and spin functionalities and thus are quite promising for future spintronic device applications.

(5) The effects of the linear laser chirp on the spin-flip and spin-transfer scenarios show that with the increase in the chirp degree the fidelity of the spin dynamics overall gets suppressed (only in rare cases can the limited enhancement of the fidelity be induced by slightly chirped lasers). However, the chirp tolerances and decline features of these scenarios are different depending on the structures and spin functionality. Generally, for the structures with the same PAH molecules, the chirp tolerance decreases in the order Fe, Co, and Ni, while for the structures with the same TM atoms, the stability order is $C_{32}H_{14} > C_{24}H_{12} > C_{10}H_8$ for Fe and Co, and reversed for Ni. Among all the structures, $Fe_2(C_{16}H_{10})$ is the most stable one with the change in laser chirp for both its spin-flip and spin-transfer scenarios. For most of the scenarios, the fidelity change trends are symmetric with respect to the chirp derivation. For the asymmetric ones, the flip scenarios are more sensitive to the positively chirped laser, while the transfer scenarios are more sensitive to the negatively chirped ones.

The results obtained in these TM-PAH molecular structures are expected to stimulate the experimental realization of spin manipulation on them, and also provide valuable insights into the relevant features of carbon-based or graphene-based magnetic structures as well as their potential applications in ultrafast nanospintronics.

ACKNOWLEDGMENTS

We acknowledge financial support from the National Natural Science Foundation of China (Grants No. 11504223 and No. 11872309) and the National Science Basic Research Plan in Shaanxi Province (Grant No. 2017JM1033).

[1] E. Beaurepaire, J.-C. Merle, A. Daunois, and J.-Y. Bigot, Phys. Rev. Lett. **76**, 4250 (1996).

[2] M. Vomir, L. H. F. Andrade, L. Guidoni, E. Beaurepaire, and J.-Y. Bigot, Phys. Rev. Lett. **94**, 237601 (2005).

[3] G. P. Zhang, W. Hübner, G. Lefkidis, Y. H. Bai, and T. F. George, Nat. Phys. **5**, 499 (2009).

[4] A. Kirilyuk, A. V. Kimel, and T. Rasing, Rev. Mod. Phys. **82**, 2731 (2010).

[5] U. Atxitia, Phys. Rev. B **98**, 014417 (2018).

[6] B. Pfau, S. Schaffert, L. Müller, C. Gutt, A. Al-Shemmary, F. Büttner, R. Delaunay, S. Düsterer, S. Flewett, R. Frömter, J. Geilhufe, E. Guehrs, C. M. Günther, R. Hawaldar, M. Hille, N. Jaouen, A. Kobs, K. Li, J. Mohanty, H. Redlin *et al.*, Nat. Commun. **3**, 1100 (2012).

[7] P. Baláž, K. Carva, U. Ritzmann, P. Maldonado, and P. M. Oppeneer, Phys. Rev. B **101**, 174418 (2020).

[8] U. Bierbrauer, S. T. Weber, D. Schummer, M. Barkowski, A.-K. Mahro, S. Mathias, H. C. Schneider, B. Stadtmüller, M. Aeschlimann, and B. Rethfeld, J. Phys.: Condens. Matter **29**, 244002 (2017).

[9] J. Chen, U. Bovensiepen, A. Eschenlohr, T. Müller, P. Elliott, E. K. U. Gross, J. K. Dewhurst, and S. Sharma, Phys. Rev. Lett. **122**, 067202 (2019).

[10] O. Morandi and P.-A. Hervieux, Phys. Rev. B **96**, 024441 (2017).

[11] H. Du, J. Liu, N. Zhang, J. Chang, W. Jin, C. Li, G. Lefkidis, and W. Hübner, Phys. Rev. B **99**, 134430 (2019).

[12] A. P. de Silva and S. Uchiyama, Nat. Nanotechnol. **2**, 399 (2007).

[13] P. Seneor, A. Bernand-Mantel, and F. Petroff, J. Phys.: Condens. Matter **19**, 165222 (2007).

[14] M. Swanson, J. T. Haraldsen, and R. S. Fishman, Phys. Rev. B **79**, 184413 (2009).

[15] F. Luis, A. Repollés, M. J. Martínez-Pérez, D. Aguilà, O. Roubeau, D. Zueco, P. J. Alonso, M. Evangelisti, A. Camón, J. Sesé, L. A. Barrios, and G. Aromí, Phys. Rev. Lett. **107**, 117203 (2011).

[16] D. Dutta, M. Becherer, D. Bellaire, F. Dietrich, M. Gerhards, G. Lefkidis, and W. Hübner, Phys. Rev. B **97**, 224404 (2018).

[17] D. Chaudhuri, G. Lefkidis, and W. Hübner, Phys. Rev. B **96**, 184413 (2017).

[18] W. Jin, M. Becherer, D. Bellaire, G. Lefkidis, M. Gerhards, and W. Hübner, Phys. Rev. B **89**, 144409 (2014).

[19] B. Lazarovits, L. Szunyogh, and P. Weinberger, Phys. Rev. B **65**, 104441 (2002).

[20] G. Pal, G. Lefkidis, and W. Hübner, Phys. Status Solidi B **247**, 1109 (2010).

[21] Y. Yagi, T. M. Briere, M. H. F. Sluiter, V. Kumar, A. A. Farajian, and Y. Kawazoe, Phys. Rev. B **69**, 075414 (2004).

[22] A. N. Andriotis, M. Menon, and G. E. Froudakis, Phys. Rev. B **62**, 9867 (2000).

[23] C. Li, J. Liu, S. B. Zhang, G. Lefkidis, and W. Hübner, Carbon **87**, 153 (2015).

[24] S. W. Poon, J. S. Pan, and E. S. Tok, Phys. Chem. Chem. Phys. **8**, 3326 (2006).

[25] K. T. Chan, J. B. Neaton, and M. L. Cohen, Phys. Rev. B **77**, 235430 (2008).

[26] Y. L. Mao, J. M. Yuan, and J. X. Zhong, J. Phys.: Condens. Matter **20**, 115209 (2008).

[27] H. Johll, H. C. Kang, and E. S. Tok, Phys. Rev. B **79**, 245416 (2009).

[28] H. C. Kandpal, K. Koepernik, and M. Richter, Phys. Rev. B **86**, 235430 (2012).

[29] L. Senapati, S. K. Nayak, B. K. Rao, and P. Jena, J. Chem. Phys. **118**, 8671 (2003).

[30] A. K. Kandalam, B. Kiran, P. Jena, X. Li, A. Grubisic, and K. H. Bowen, J. Chem. Phys. **126**, 084306 (2007).

[31] Y. Wang, J. Szczepanski, and M. Vala, Chem. Phys. **342**, 107 (2007).

[32] X. Li, S. Eustis, K. H. Bowen, A. K. Kandalam, and P. Jena, J. Chem. Phys. **129**, 074313 (2008).

[33] A. K. Kandalam, P. Jena, X. Li, S. N. Eustis, and K. H. Bowen, J. Chem. Phys. **129**, 134308 (2008).

[34] A. Simon, M. Rapacioli, M. Lanza, B. Joalland, and F. Spiegelman, Phys. Chem. Chem. Phys. **13**, 3359 (2011).

[35] X. Li, K. H. Bowen, P. Jena, and A. K. Kandalam, J. Chem. Phys. **135**, 204301 (2011).

[36] L.-P. Ding, X.-Y. Kuang, P. Shao, and M.-M. Zhong, Dalton Trans. **42**, 8644 (2013).

[37] M. Mahmoodinia, P.-O. Åstrand, and D. Chen, J. Phys. Chem. C **119**, 24425 (2015).

[38] T. Alonso-Lanza, Á. Mañanes, and A. Ayuela, J. Phys. Chem. C **121**, 18900 (2017).

[39] A. N. Rudenko, F. J. Keil, M. I. Katsnelson, and A. I. Lichtenstein, Phys. Rev. B **86**, 075422 (2012).

[40] N. Zhang, H. Du, J. Chang, W. Jin, C. Li, G. Lefkidis, and W. Hübner, Phys. Rev. B **98**, 104431 (2018).

[41] L. Sheng, Y. Ono, and T. Taketsugu, J. Phys. Chem. C **114**, 3544 (2010).

[42] M. K. Srivastava, Y. Wang, A. F. Kemper, and H.-P. Cheng, Phys. Rev. B **85**, 165444 (2012).

[43] X. J. Liu, C.-Z. Wang, H.-Q. Lin, M. Hupalo, P. A. Thiel, K.-M. Ho, and M. C. Tringides, Phys. Rev. B **90**, 155444 (2014).

[44] H. Nakatsuji, Chem. Phys. Lett. **67**, 329 (1979).

[45] M. J. Frisch, G. W. Trucks, H. B. Schlegel, G. E. Scuseria, M. A. Robb, J. R. Cheeseman, G. Scalmani, V. Barone, G. A. Petersson, H. Nakatsuji, X. Li, M. Caricato, A. V. Marenich, J. Bloino, B. G. Janesko, R. Gomperts, B. Mennucci, H. P. Hratchian, J. V. Ortiz, A. F. Izmaylov *et al.*, Gaussian 16, Revision B.01, Gaussian Inc., Wallingford, CT, 2016.

[46] W. Jin, F. Rupp, K. Chevalier, M. M. N. Wolf, M. C. Rojas, G. Lefkidis, H.-J. Krüger, R. Diller, and W. Hübner, Phys. Rev. Lett. **109**, 267209 (2012).

[47] R. Gómez-Abal, O. Ney, K. Satitkovitchai, and W. Hübner, Phys. Rev. Lett. **92**, 227402 (2004).

[48] P. P. Wang, M. Y. Qiu, X. Lu, W. Jin, C. Li, G. Lefkidis, and W. Hübner, Phys. Rev. B **101**, 104414 (2020).

[49] J. R. Cash and A. H. Karp, ACM Trans. Math. Softw. **16**, 201 (1990).

[50] T. Hartenstein, C. Li, G. Lefkidis, and W. Hübner, J. Phys. D: Appl. Phys. **41**, 164006 (2008).

[51] See Supplemental Material at http://link.aps.org/supplemental/10.1103/PhysRevB.103.054433 for detailed information on geometries, infrared spectra, energy levels with the inclusion of singlet states, information of the initial and final states for the achieved spin dynamics, and the chirp effect on the spin-flip scenario in $Fe_2(C_{16}H_{10})$, which includes Refs. [70–72].

[52] M. Tanveer, J. Dorantes-Dávila, and G. M. Pastor, Phys. Rev. B **96**, 224413 (2017).

[53] R. J. Xiao, D. Fritsch, M. D. Kuz'min, K. Koepernik, M. Richter, K. Vietze, and G. Seifert, Phys. Rev. B **82**, 205125 (2010).

[54] C. Cao, M. Wu, J. Z. Jiang, and H. P. Cheng, Phys. Rev. B **81**, 205424 (2010).

[55] G. Forte, A. Grassi, G. Lombardo, A. La Magna, G. Angilella, R. Pucci, and R. Vilardi, Phys. Lett. A **372**, 6168 (2008).

[56] M. D. Morse, G. P. Hansen, P. R. R. Langridge-Smith, L. S. Zheng, M. E. Geusic, D. L. Michalopoulos, and R. E. Smalley, J. Chem. Phys. **80**, 5400 (1984).

[57] R. Pou-Amérigo, M. Merchán, I. Nebot-Gil, P.-Å. Malmqvist, and B. O. Roos, J. Chem. Phys. **101**, 4893 (1994).

[58] J. C. Pinegar, J. D. Langenberg, C. A. Arrington, E. M. Spain, and M. D. Morse, J. Chem. Phys. **102**, 666 (1995).

[59] D. Chaudhuri, G. Lefkidis, A. Kubas, K. Fink, and W. Hübner, in *Ultrafast Magnetism I*, edited by J. Y. Bigot, W. Hübner, T. Rasing, and R. Chantrell, Springer Proceedings in Physics Vol. 159 (Springer, Cham, Switzerland, 2015), pp. 159–161.

[60] S. Paranthaman, Croat. Chem. Acta **90**, 17 (2017).

[61] C. D. Dong, G. Lefkidis, and W. Hübner, Phys. Rev. B **88**, 214421 (2013).

[62] C. D. Dong, G. Lefkidis, and W. Hübner, J. Supercond. Novel Magn. **26**, 1589 (2013).

[63] W. Jin, C. Li, G. Lefkidis, and W. Hübner, Phys. Rev. B **89**, 024419 (2014).

[64] S. Ibáñez, A. Peralta Conde, D. Guéry-Odelin, and J. G. Muga, Phys. Rev. A **84**, 013428 (2011).

[65] P. Kumar and A. K. Sarma, Phys. Rev. A **87**, 025401 (2013).

[66] V. A. Astapenko and M. S. Romadanovskii, Laser Phys. **19**, 969 (2009).

[67] Z. Ghaedi, M. Hosseini, and F. Sarreshtedari, Opt. Commun. **431**, 109 (2019).

[68] G. P. Zhang, G. Lefkidis, W. Hübner, and Y. H. Bai, J. Appl. Phys. (Melville, NY) **111**, 07C508 (2012).

[69] G. Lefkidis and W. Hübner, in *Ultrafast Magnetism I*, edited by J. Y. Bigot, W. Hübner, T. Rasing, and R. Chantrell, Springer Proceedings in Physics Vol. 159 (Springer, Cham, Switzerland, 2015), pp. 128–130.

[70] K. Ohno and H. Shinohara, J. Mol. Struct. **352-353**, 475 (1995).

[71] A. L. Mattioda, A. Ricca, J. Tucker, C. W. Bauschlicher, and L. J. Allamandola, Astron. J. **137**, 4054 (2009).

[72] S. Öttl, S. E. Huber, S. Kimeswenger, and M. Probst, Astron. Astrophys. **568**, A95 (2014).